arXiv:astro-ph/0103030v2 26 Apr 2001

Distributions of secondary muons at sea level from cosmic gamma rays below 10 TeV

J. Poirier, [a] S. Roesler, [b] A. Fassò [c]

[a] *Center for Astrophysics, Physics Department, University of Notre Dame, Notre Dame, Indiana 46556, USA*

[b] *Stanford Linear Accelerator Center, MS. 48, 2575 Sand Hill Road, Menlo Park, California 94025, USA*
Tel.: +1-650-926-2048, Fax: +1-650-926-3569
Email: sroesler@slac.stanford.edu

[c] *CERN-EP/AIP, CH-1211 Geneva 23, Switzerland*

Abstract

The FLUKA Monte Carlo program is used to predict the distributions of the muons which originate from primary cosmic gamma rays and reach sea level. The main result is the angular distribution of muons produced by vertical gamma rays which is necessary to predict the inherent angular resolution of any instrument utilizing muons to infer properties of gamma ray primaries. Furthermore, various physical effects are discussed which affect these distributions in differing proportions.

Key words: air shower simulation, gamma rays, muons
PACS: 95.75.Pq, 98.70.Sa, 98.70.Rz, 13.60.Le

1 Introduction

Muons detected at ground level arise mainly as decay products of charged mesons. These mesons are created abundantly in hadronic showers, most of which are caused by primary cosmic ray protons and nuclei interacting inelastically with the nuclei of the atmosphere. A small fraction of muons, however, have their first origin in photonuclear reactions induced by primary or secondary cosmic gamma rays. Several authors have performed analytical or Monte Carlo calculations of the muon flux produced in gamma showers (see references [10-21] of [1]). Most of these calculations were one dimensional and all of them referred to gamma energies much larger than 10 TeV.

Despite their relative scarcity compared to the large background of muons from hadron-generated showers, muons originating from primary gamma ray interactions are important for ground-based high statistics cosmic ray experiments which are sensitive to energies ≤ 10 TeV such as MILAGRO [2] and GRAND [3]. Cosmic gamma rays, unlike charged hadrons, are unaffected by the Earth's and galactic magnetic fields and their direction points directly to the location of their source. Therefore, an accumulation of muon directions around a particular angle (and also at a particular time in the case of pulsed sources or gamma ray bursts) carries direct information about the location of the source and the neutrality of the primary causing the excess. The ability to distinguish these muons from background muons depends upon statistics, the strength and energy spectrum of the emitting source, the angular resolution of the experiment, and the degradation of the angular resolution due to all the physical processes which occur between the primary and the muon at detection level. This last point is the focus of this calculation. Knowledge of this angular resolution is important in order to determine a detection window which is large enough to include a good fraction of the gamma signal and, at the same time, small enough to minimize the large uniform background of hadronic origin.

The information about the primary gamma direction is degraded by multiple physical processes so the final measured direction of the muon is no longer collinear with the primary which originated the muon's ancestors. In particular, the direction resolution is affected by the angle of production of the mesons in the primary interaction (and then in subsequent hadronic interactions of these mesons to create additional mesons), the decay angle of the muon relative to its parent meson, and the lengths of the charged particle paths including that of the detected muon at ground level. Along these path lengths there is Coulomb scattering and deflection in the Earth's magnetic field for the trajectories of the mesons and the muon (usually most important for the muon which typically has the longest flight path and the lowest momentum.) In addition, these effects depend upon the energy of the particles involved and on the varying properties of the atmosphere (pressure, temperature.) The muons are produced by mesons of second, third, or further generations. The number of generations typically increases with increasing primary gamma energy and each new generation involves an additional production angle which tends to increase the angular disparity between muon and primary because of more steps in a random walk type process. An opposing effect at higher energies is that all angular distributions are more forward-peaked thus decreasing the angular disparity; the resulting effect is a combination of the two.

The purpose of the present study is to estimate the influence of the various effects on the ultimate angular resolution which can be obtained utilizing ground level muons. The complexity of the problem requires detailed analyses which can only be obtained by a full three-dimensional Monte Carlo (MC)

calculation. In addition, since only a small fraction of all primary photons gives rise to an event of interest, it is desirable to resort to statistical variance reduction techniques to bring the computing task within manageable limits.

The Monte Carlo program FLUKA [4–7] provides an accurate and well-tested description of the hadronic and electromagnetic interactions with all the relevant physical effects, and a set of effective statistical tools to accelerate convergence of the results. The program has been used to calculate the geometrical properties of secondary muons at sea level arising from primary gamma cosmic rays with energies from 1 GeV to 10 TeV interacting in the Earth's atmosphere. In this energy range the cross section for direct muon pair production is much smaller than that for hadroproduction and has been neglected. This range has been shown in [1] to be the interval which produces the maximum secondary muon flux at ground level for primary differential gamma spectra with spectral indices larger than 2.4 (a smaller index would yield a harder spectrum and give a maximum secondary muon flux arising from primary energies beyond those considered here.)

In this paper, only incident cosmic gamma rays at perpendicular (vertical) incidence on top of the atmosphere are considered. Ground-based experiments often choose angles close to normal for reasons of simplicity and because the detection rate is a maximum, the rate dropping rather rapidly as the angle deviates markedly from normal. For small angles from normal, the angular resolution results will probably not differ significantly from those presented in this paper.

In addition to the angular correlation of secondary muons at ground level, this study provides also additional information such as the distribution of heights at which the muons originate, the muon's kinetic energy distribution at the ground and production level, the radial distribution of the muons, and the number of generations which preceded that of the muon.

2 Air shower calculations with FLUKA

The 2000 version of the FLUKA Monte Carlo code was used to simulate the electromagnetic and hadronic particle cascades induced by primary gamma rays in the atmosphere. The powerful biasing capabilities of the code allowed a simulation of the full three-dimensional shower in a single run from the top of the atmosphere down to ground level.

The physical models implemented in FLUKA which are relevant for the present study as well as various variance reduction techniques were already discussed in [1]. There it was emphasized that these models were validated

by comprehensive comparisons of FLUKA results with experimental data obtained mostly at accelerators but also in recent cosmic ray studies [8–11]. Nevertheless, the simulation of an atmospheric shower and, in particular, of its muon component is a relatively new area of application of FLUKA. Additional examples showing that the code allows remarkably accurate predictions in this area are given in Section 2.1. Section 2.2 contains some details of the present gamma ray shower simulations which supplement those discussed in [1]; this reference contains a more complete description.

2.1 Muon production in air showers induced by hadronic primaries and comparison to experimental data

No data exist for the muon component of gamma ray-induced showers to which FLUKA results could be directly compared. On the other hand, data on muon flux and energy spectra have become available recently for atmospheric showers induced by cosmic ray protons and nuclei. These data were mostly obtained with spectrometers in balloon-borne experiments and cover the whole range of atmospheric depths from the top of the atmosphere down to sea level.

Fortunately, the mechanisms and models for muon production and transport in gamma ray-induced showers are largely the same as those in pure hadronic air showers. In both cases, the production of the pions which eventually decay into muons is described by the Dual Parton Model (DPM) [12]. The only difference is that in the former case the photon is assumed to fluctuate first into a quark-antiquark state which then interacts hadronically, identical to a meson. This so-called Vector Meson Dominance model (VMD) for the hadronic photon fluctuation is a well-established concept (see [13] and references therein) and its application together with the DPM to hadronic interactions of photons has been proven to be very successful (see, for example, [14,15]). A good description of muon production from proton- and nuclei-induced air showers should therefore give confidence that the corresponding results obtained with FLUKA for photon-induced air showers are reliable as well. In the following a few examples are given.

A critical aspect of muon production in the atmosphere is the dependence of the total muon flux on the height above sea level. This dependence is commonly expressed as a function of depth in the atmosphere (in g/cm^2 of air) which is a measure of the amount of air penetrated by the cascade. It has been measured by the CAPRICE experiment which was able to distinguish between positively and negatively charged muons. Results obtained with FLUKA for negative muons are compared with CAPRICE data [16] in Fig. 1. The different curves correspond to the muon flux calculated for different intervals of the muon momentum. To correspond to the average geometrical response of

the CAPRICE apparatus, only muons with a polar angle of less than 9° with respect to the vertical (i.e., vertical muons) were scored. The simulations are based on sophisticated models and methods for the sampling of the identity, energy, and angle of the hadronic primary from the distributions of galactic cosmic rays on top of the atmosphere at the time of the measurements. More details can be found in [10,17]. As can be seen from the figure, FLUKA gives a good description of the negative muon flux for all depths. Similar agreement exists for positive muons (not shown here).

Energy spectra of muons were recorded by the same experiment at ground (i.e., at an atmospheric depth of 886 g/cm^2) [18]. FLUKA results for positive and negative muons are compared to these data in Fig. 2a. Again, good agreement between simulation and data is found.

Finally, the ratio of the fluxes of positively and negatively charged muons is compared to CAPRICE data [18] in Fig. 2b. Data and calculations are again for vertical muons at a depth of 886 g/cm^2. The ratios are plotted as a function of the muon energy.

The above comparisons of FLUKA results and experimental data together with those published in earlier studies [8–11] indicate that the application of FLUKA to cosmic gamma ray showers should give reliable predictions as well.

2.2 The Monte Carlo simulation of cosmic gamma ray showers

In order to study the dependence of the shower properties on the primary photon energy, the showers were calculated for monoenergetic photons impinging vertically on top of the atmosphere (taken to be 80 km above sea level). In total 9 sets of simulations were performed for the following primary energies: 1, 3, 10, 30, 100, 300, 1000, 3000, and 10000 GeV. As in the earlier study [1] the atmosphere was approximated by 50 layers with a constant density in each layer and with layer-densities decreasing exponentially with increasing altitude. It has been verified [1] that this approximation does not affect the conclusions drawn in this study. The geometry is described in a right-handed orthogonal system with its origin at the intersection of the shower axis with sea-level elevation, z points to the center of the Earth and x and y point North and East, respectively. Most of the results discussed throughout the paper were obtained without the effect of the magnetic field of the Earth included. However, for two primary energies (10 GeV and 1 TeV) additional simulations were performed which included the magnetic field of three different geographical locations (see Sec. 3.4).

The use of several variance reduction (biasing) techniques was essential to obtain results with reasonable statistical significance. They included leading

particle biasing at each electromagnetic interaction, biasing of the photon mean-free-path with respect to photonuclear interactions, biasing of the decay length of charged mesons, and particle splitting at the boundaries of different air layers. Each of these biasing techniques alters the statistical weight of a particle in the cascade. A muon as produced and transported in the Monte Carlo simulation and which carries a certain statistical weight (hereafter called "MC muon") contributes to distributions, yields, etc., of actual, i.e., measurable muons with a probability equal to its weight. The use of biasing techniques would not be appropriate to study fluctuations within the same shower which, however, is not the aim of this study. More details on the biasing techniques can be found in [1].

For each MC muon reaching sea level (detection level) the following information was recorded in a file for later analysis:

(1) Information on the muon at detection level: muon charge, lateral coordinates (x, y) with respect to shower axis, direction cosines with respect to the x and y axes, kinetic energy, statistical weight of the muon, and number of the event (i.e., primary cosmic ray photon) which produced this muon.
(2) Information on the muon at its production vertex (i.e., meson decay vertex): lateral coordinates (x, y) with respect to shower axis, direction cosines with respect to the x and y axes, height z, kinetic energy, statistical weight of the muon, and identity of the decaying meson.
(3) Information on the grandparent at the parent production vertex: particle identity, lateral coordinates (x, y) with respect to shower axis, direction cosines with respect to the x and y axes, height z, kinetic energy, statistical weight of the particle, and generation number.
(4) Information on the photonuclear interaction vertex preceding the hadronic cascade in which the muon at detection level has been created: lateral coordinates (x, y) with respect to shower axis, direction cosines with respect to the x and y axes, height z, energy, statistical weight of the photon, and generation number of the photon

The generation of a particle increases with each sampled discrete interaction (electromagnetic or hadronic), i.e., the primary photon is generation "1," the generation of the electron and positron after the first pair production process would be "2," etc. Delta ray production and Coulomb scattering are not considered to increase the generation number.

A summary of the simulated particles cascades for each primary gamma ray energy is given in Table 1. In the following, all results refer to the sum of positive and negative muons. The number of histories (number of primary gamma rays), N_γ, calculated for each primary energy decreases with energy in order to obtain uniform statistical significance on the muons which reach ground level

for the different primary energies. At the lowest energy (1 GeV) the muon flux per gamma at sea level is very small so that even with a significant amount of biasing in the simulations it is difficult to reach adequate statistics. Less emphasis was therefore put on the simulation at 1 GeV. The column N_μ gives the total number of muons reaching detection level for the given number of primary photons N_γ. The predictions for the muon multiplicity at sea level per incident primary gamma ray N_μ/N_γ are listed in the last column. Similar values were already reported in [1], however with smaller statistical significance than those in Table 1.

Table 1
Summary of the simulated particle cascades. N_γ is the number of histories calculated for each primary energy (E_γ) and N_μ is the total number of muons (i.e., the sum of the weights) scored at sea level. In the last column the average muon multiplicity per primary gamma ray is given. The errors quoted in the last column represent the statistical uncertainties of the calculations.

E_γ (GeV)	N_γ	N_μ	N_μ/N_γ
1	4542000	3.78×10^{-3}	$(8.32 \pm 0.46) \times 10^{-10}$
3	26000000	117.7	$(4.53 \pm 0.23) \times 10^{-6}$
10	2250000	1191	$(5.29 \pm 0.03) \times 10^{-4}$
30	1260000	3843	$(3.05 \pm 0.01) \times 10^{-3}$
100	800000	11351	$(1.42 \pm 0.01) \times 10^{-2}$
300	324445	17259	$(5.32 \pm 0.02) \times 10^{-2}$
1000	143131	31709	$(2.22 \pm 0.01) \times 10^{-1}$
3000	27040	21954	$(8.12 \pm 0.05) \times 10^{-1}$
10000	18000	58874	3.27 ± 0.03

3 Angular correlations

3.1 Angular distribution of muons at sea level

In this section the effect of the Earth's magnetic field is not included; Section 3.4 has a separate discussion of this added effect which depends on the geographical location of interest. Fig. 3 summarizes the deviations of the angle of the muons which reach sea level from the primary gamma direction (vertical angle). It shows the distribution of the angle Θ_{xz} which is the muon's angle with respect to the z axis projected onto the xz plane (North-down plane).

This angle is defined as $\Theta_{xz} = \arctan(\cos\theta_x/\cos\theta_z)$ where $\cos\theta_x$ and $\cos\theta_z$ are the direction cosines of the detected muon. Negative projections have been reflected upon the positive values for Θ_{xz} since positive and negative angles would be symmetric in the absence of the magnetic field. Also, the distributions in the yz plane (East-down plane) are similar to those shown in Fig. 3.

Since the angle of the primary gamma with respect to the z axis is zero (vertically incident primaries), any deviation of the muon direction from zero degrees is due to the various interaction and transport processes occurring in the cascade between the primary gamma ray and the muon which reaches sea level. Thus the results shown in Fig. 3 represent the correlation between the direction of the detected muon and the direction of the primary gamma ray.

All distributions in Fig. 3 are normalized to unit area to compare their shapes. The shape of the distributions for primary energies above about 30 GeV varies rather slowly. Therefore, only two histograms (100 GeV and 10 TeV) are shown for this energy range. At lower energies the shape of the distributions changes significantly as can be seen from the histograms for 3 and 10 GeV. The distributions become wider with decreasing primary energy. At low primary gamma ray energies, the muons have, on average, lower energies which cause larger angular deviations from the primary due to kinematics and scattering effects which are larger for the lower energies. This is illustrated in Fig. 4 for primary energies of 10 GeV and 10 TeV. An arbitrary cut of 2 GeV was applied to the angular distributions so that contributions from muons with energies below and above this cut could be seen separately along with the total.

Two measures of the widths of these distributions as a function of the energy of the incident primary cosmic gamma ray are given in Table 2. The width parameters are: the half-width at half-maximum-height (HWHM) and the angular half-width containing 68% of the muons, i.e., the same number of events that a 1σ cut would include if the distributions had a Gaussian shape (which they don't have, because of the long tails). Both of these parameters provide a measure of the distribution widths which minimizes the distorting effect of a tail. In addition, the values for various cuts on the kinetic energy of the detected muons (1, 2, and 4 GeV) are presented. The cutoff energy results for primary energies of less than 10 GeV were omitted due to lack of statistics. For the HWHM calculation, the maximum height is assumed to be the value in the first bin of the corresponding histogram, i.e., the average value in the interval $|\Theta_{xz}| < 0.25$ degrees. The x and y rectangular coordinate system was chosen to represent the results of the muon's angular distribution as the corrections for the additional deflection due to the Earth's magnetic field differ in these two directions. In addition, (x, y) is the natural coordinate system for GRAND. For some experiments a space angle is more natural. If we define $R = \sqrt{x^2 + y^2}$, then the space angle resolution ($\delta\Theta_R$(HWHM)) can be estimated directly from the numbers in Table 2 by multiplying the

Table 2
Half-width at half-maximum-height ($\delta\Theta_{xz}$(HWHM)) of the angular distributions and angular half-width containing 68% of the muons ($\delta\Theta_{xz}$(68%)). For both quantities the values are given for all muon energies and for muon kinetic energies above 1, 2, and 4 GeV. Units of the widths are in degrees.

	$\delta\Theta_{xz}$(HWHM)			
E_γ (GeV)	$E_\mu > 0$	$E_\mu > 1$ GeV	$E_\mu > 2$ GeV	$E_\mu > 4$ GeV
1	31.0	–	–	–
3	8.20	–	–	–
10	3.23	2.95	2.57	1.87
30	1.87	1.73	1.59	1.35
100	1.12	1.04	0.95	0.81
300	0.92	0.85	0.77	0.66
1000	0.91	0.82	0.74	0.63
3000	0.98	0.89	0.78	0.66
10000	1.05	0.94	0.82	0.67
	$\delta\Theta_{xz}$(68%)			
1	28.3	–	–	–
3	7.36	–	–	–
10	3.83	3.06	2.46	1.66
30	3.07	2.40	1.95	1.45
100	2.87	2.15	1.69	1.21
300	3.04	2.18	1.68	1.16
1000	3.32	2.31	1.75	1.19
3000	3.62	2.42	1.81	1.23
10000	4.05	2.57	1.89	1.27

$\delta\Theta_{xz}$(HWHM) values by $\sqrt{2}$ due to the symmetry of x and y in the absence of a magnetic field.

As can be seen in this table: (i) as the primary energy decreases below 10 GeV, the width of the angular distribution increases dramatically, (ii) as the energy rises above 300 GeV, there is only a small, gradual increase in the width of the angular distribution, and (iii) the width of the distribution narrows as the muon's cutoff energy is raised; i.e., the angular resolution becomes better by eliminating the lower energy muons which have, on average, poorer angular

resolution.

3.2 Correlation of muon angle with distance from the shower axis

In the preceding section, angular distributions were given for all muons regardless of their lateral distance from the shower axis. However, as the distance from the shower axis increases, the angle is systematically biased away from the shower axis. Fig. 5 shows the correlation between the projected angle Θ_{xz} and the x coordinate (i.e., the northward distance from the shower core) of the muon position at sea level for primary gamma ray energies of 10 GeV and 1 TeV. The angular distributions are given for different intervals in x and each distribution is normalized to unit area. Here, negative values of Θ_{xz} have not been reflected onto positive values and are explicitly shown. As expected, the peak of the Θ_{xz} distributions are shifted toward positive values as x becomes more positive and the distributions become wider as x increases. Both effects depend on the energy of the primary gamma ray and are more pronounced at higher energies.

Hence, the angular distributions narrow significantly if they are limited to muons within a certain interval around the shower axis. Information on this correlation between the angle and the lateral distance of the muon from the shower axis allows experiments to improve the angular resolution by applying cuts to the data, e.g., in x. If the available statistics demand using all available muons, their angle at large x's (y's) could be corrected by the most probable angle at that x (or y) to obtain a better estimate of the primary's direction.

This correlation can also be used to infer the height from which the muon originated, a parameter difficult to obtain experimentally. If one extrapolates the muon direction backward (upward), the intersection point with the centroid of the shower (which can be obtained from the more numerous electrons in the same shower), is an estimator for the height where the muon was created. However, deviations of the muon production vertex from the centroid and the physical processes which alter the muon track between the production vertex and sea level obscure this information somewhat. For this reason it is not possible to study this question on a muon-by-muon basis. For example, tracks with projected angles close to zero which exist at almost all x-distances from the origin would yield, upon extrapolation, an infinite height-of-origin. This problem can be circumvented by finding the mean x within an interval of x and dividing this mean by the corresponding mean of $\tan\Theta_{xz}$. The averaging serves another purpose as well: the randomness of the various physical processes, such as scattering, tend to cancel in the averaging.

3.3 Angular resolution for a spectrum of primary gamma ray energies

The results of the preceding sections can be combined to obtain the expected angular resolution for a spectrum of primary gamma rays. Various steps in the calculation are shown in Fig. 6a. Here, a differential energy spectrum $d\Phi_\gamma/dE_\gamma \propto E_\gamma^{-\alpha}$ with a spectral index of $\alpha = 2.41$ is assumed; this α corresponds to the average of the spectral indices reported in the Third EGRET Catalog [19]. Folding $d\Phi_\gamma/dE_\gamma$ with the number of muons reaching sea level per primary photon, N_μ/N_γ, yields the number of muons at sea level as function of the primary gamma ray energy, $d\Phi_\mu/dE_\gamma$, with $\Phi_\mu = N_\mu/N_\gamma \times \Phi_\gamma$. Note that the differential spectra in Fig. 6a are multiplied by E_γ.

The flatness of the differential muon flux per gamma at sea level ($E_\gamma \times d\Phi_\mu/dE_\gamma$) above 10 GeV signifies that the muons originate rather uniformly from a broad range of primary energies. Below 10 GeV, the muon flux decreases steeply as N_μ/N_γ rapidly approaches zero. Harder spectral indices ($\alpha < 2.41$) would enhance the muon flux from higher primary energies and, conversely, softer indices would enhance lower energies.

Furthermore, in Fig. 6a the half-widths at half-maximum-height $\delta\Theta_{xz}$ (HWHM) (given in Table 2 in the "$E_\mu > 0$" column) are plotted. These widths are multiplied by the differential muon flux which is also shown in Fig. 6a. As can be seen, the larger angular widths at the lower energies ($E_\gamma < 3$ GeV) do not contribute due to the small sea level muon flux at these energies.

The average angular resolution (i.e., average angular width) in the North-down plane, $\langle\delta\Theta_{xz}(\mathrm{HWHM})\rangle$, for a differential gamma ray spectrum with an index α is obtained from

$$\langle\delta\Theta_{xz}(\mathrm{HWHM})\rangle = \frac{\int \delta\Theta_{xz} \times N_\mu/N_\gamma \times E_\gamma^{-\alpha}\, dE_\gamma}{\int N_\mu/N_\gamma \times E_\gamma^{-\alpha}\, dE_\gamma} \tag{1}$$

and shown in Fig. 6b. As can be seen, the resolution is about constant (1°) up to a spectral index of 2 and then rises for larger indices due to the increasing importance of the wider angular widths at low energy.

3.4 Effect of the magnetic field

The magnetic field of the Earth deflects positively (negatively) charged particles primarily eastward (westward) causing the angular distributions in the projected angle Θ_{yz} (i.e., projected onto the East-down plane) to become wider. The size of the effect depends on the strength and direction of the

field and, therefore, varies with geographic location. To obtain a measure of the magnitude of the added angular widths and how it depends on geographic location, three different locations are considered and summarized in Table 3. In order to estimate the maximum possible deflection, a location of maximum northward field component was chosen. Due to the offset of the magnetic field axis from the Earth's center, this location is at about 9°N, 100°E (below referred to as "maximum"). In addition, two locations with intermediate magnetic fields were chosen: 42°N, 86°W (GRAND) and 36°N, 106°W (MILAGRO). The magnetic field components for these locations were obtained from the latest revision of the International Geomagnetic Reference Field (IGRF) [20] and are listed in Table 3. Here, the components of the magnetic field, B, are given in nanotesla (nT) and the components B_x, B_y, B_z are directed North, East, and toward the center of the Earth, respectively. For uniformity of comparison, all values are for sea level elevation.

Table 3
Earth's magnetic field components B_x (North), B_y (East), and B_z (vertically downward) in nanotesla for the three considered locations. The field has been obtained from the IGRF2000 model [20]. For a given location the field components vary only by $\leq 4\%$ for heights of 0 to 80 km. Here, the values are given for sea level and a date in Feb., 2001.

Location	B_x (nT)	B_y (nT)	B_z (nT)
(1) GRAND, 42°N, 86°W	18592	-1361	52547
(2) MILAGRO, 36°N, 106°W	22751	4141	46241
(3) Maximum, 9°N, 100°E	41407	-211	1326

FLUKA is able to transport particles in arbitrary magnetic fields. However, since the variation of the field in the atmosphere with height above sea level and with time is only minor (about 4%), for simplicity the magnetic field used in the calculation for a certain location was assumed to be constant throughout the whole geometry. In addition, although the MILAGRO experiment is located at a height of 2170 m above sea level, all results reported for that location refer to sea level as this allows a direct comparison to the results at the other locations.

The angular distributions at sea level for the three magnetic field conditions and for primary gamma ray energies of 10 GeV and 1 TeV are shown in Fig. 7. In addition, the distributions obtained without magnetic field are given. As can be seen, for a 10 GeV gamma primary, the effect of the Earth's magnetic field is considerable and changes with geographic location; as the northward component of the magnetic field increases, the width increases. However, at 1 TeV, there is only a slight widening of the distributions with increasing the North component of the field. To within the statistical uncertainties of the

calculations, the total number of muons which reach sea level per primary gamma ray is independent of the effect of the Earth's magnetic field for the two energies studied in this section (10 GeV and 1 TeV).

The half-widths of the angular distributions in the North-down (Θ_{xz}) and East-down planes (Θ_{yz}) containing 68% of the muons are presented for the different locations in Table 4. Again, the widths are given for distributions

Table 4
The half-widths of the muon's sea level angular distributions which contain 68% of the muons and their dependence on the magnetic field strength. Results are presented for three different geographic locations: (1) 42°N, 86°W (GRAND), (2) 36°N, 106°W (MILAGRO), and (3) 9°N, 100°E (maximum) in order of increasing values of B_x. For each location the widths are given for the projected angles onto the North-down (labeled "N-d.") and East-down (labeled "E-d.") planes. The reference values from the calculations with no magnetic field (labeled "n.f.") are also shown; here, the small differences between North-down and East-down are only statistical fluctuations. Widths are listed for muon kinetic energies above 0 (all), 1, 2, and 4 GeV for primary gamma energies of 10 and 1000 GeV. The additional column for $E_\mu > 0$ gives the widths in the East-down plane of the muons at their production vertex ("birth", labeled "b"). Units of the widths are in degrees.

	E_γ	$E_\mu > 0$			$E_\mu > 1$ GeV		$E_\mu > 2$ GeV		$E_\mu > 4$ GeV	
	(GeV)	N-d.	E-d.	E-d.(b)	N-d.	E-d.	N-d.	E-d.	N-d.	E-d.
n.f.	10	3.83	3.84	3.41	3.06	3.06	2.46	2.45	1.66	1.64
	1000	3.32	3.32	3.03	2.31	2.30	1.75	1.74	1.19	1.19
(1)	10	3.85	4.41	3.38	3.06	3.53	2.47	2.88	1.67	2.03
	1000	3.31	3.48	3.0	2.30	2.42	1.74	1.84	1.19	1.26
(2)	10	3.89	4.73	3.40	3.09	3.83	2.48	3.15	1.67	2.25
	1000	3.33	3.61	3.02	2.32	2.52	1.75	1.91	1.19	1.30
(3)	10	3.86	6.44	3.38	3.05	5.28	2.44	4.44	1.64	3.34
	1000	3.32	4.19	3.02	2.31	2.93	1.74	2.24	1.20	1.56

containing only muons above certain kinetic energy thresholds (including zero threshold, or no cut). In addition, the corresponding values from the calculations without the effect of the magnetic field are given. The widths in the North-down plane are much less affected than in the East-down plane which contains the dominant effect of the magnetic deflection. This effect increases with increasing values of B_x or decreasing values of muon momentum. In addition to the widths of the muon's sea level angular distributions, Table 4 also shows the values at their production vertex (birth, E-d.(b)). Interestingly, these values are almost constant for the different field conditions. The effect

of the magnetic field on the angular distributions is therefore mainly the deflection of the muon over its longer path and not the deflection of the parent pions or other charged particles preceding in the cascade due to their shorter path lengths and higher momenta as compared to the muons. In addition, the dominant factor in the final width (except for the highest magnetic field value) is the muon's angular distribution at its production (birth) point.

4 The effect of pressure and temperature variations

Air pressure and temperature changes cause small variations in the density profile of the atmosphere and thus affect the muon flux at sea level. In order to obtain a quantitative estimate of these two effects, the following cases were studied: (i) the air density in each layer was increased by 3% while all other variables (geometry, cutoffs, etc.) were kept constant and (ii) the height above sea level of each slab boundary was raised by 5% and the corresponding density decreased in the same proportion such that the total thickness of air (in g/cm^2) above the surface of the Earth remained constant. The former modification simulates an air pressure increase (p) whereas the latter simulates an overall 5% increase in absolute temperature (T) of the atmosphere. Since muons are produced at atmospheric heights far above those which determine the weather at the surface of the Earth, the mean T which is involved in this calculation has little correlation with the temperature at the Earth's surface. Thus the temperature effect calculated here is not expected to correlate with the Earth's surface temperature but would require temperature measurements of the Earth's atmosphere averaged from 0 to 20 km above the Earth's surface as obtained, for example, in weather balloon measurements. The results presented in this section allow an investigation of, or corrections for, the muon flux due to small variations in the atmospheric pressure and height-averaged temperature.

The results for the total muon yield per primary gamma ray are summarized for two energies (10 GeV and 1 TeV) in Table 5. In all cases the muon yields decreased by 3% to 6%, the decrease being more pronounced at the lower energy. As for increased pressure, a higher density increases the interaction probability of the pions and thus decreases the probability of decay, i.e., fewer muons are produced. As well, the added thickness of air which the muons must traverse is a barrier which some will fail to overcome. On the other hand, raising the boundaries of the layers and reducing their density causes two counterbalancing effects: (i) the pions propagate in a less dense medium and thus have a greater probability to decay rather than interact thus producing more muons, and (ii) the muons must propagate longer distances resulting in a greater probability that they will decay before reaching ground level. The calculated temperature dependence of the muon multiplicity ratio suggests

Table 5
Summary of the effect of pressure and temperature variations on the average muon multiplicity per primary gamma ray at detection level, N_μ/N_γ. The column labeled "ref. atmosphere" repeats the values listed in Table 1 for the reference problem. The "5% temperature increase" corresponds to an average increase in the absolute temperature profile from 0 to 80 km.

E_γ	Muon multiplicity per primary gamma ray, N_μ/N_γ		
(GeV)	ref. atmosphere	3% density increase	5% temperature increase
10	$(5.29 \pm 0.03) \times 10^{-4}$	$(5.08 \pm 0.02) \times 10^{-4}$	$(4.97 \pm 0.02) \times 10^{-4}$
1000	0.221 ± 0.001	0.214 ± 0.001	0.213 ± 0.001

that the enhanced muon decay probability dominates at these energies and is the more dominant at the lower energy.

5 General properties of muon production in gamma ray showers

Information on the muons at sea level and on their ancestors (i.e., the parent, grandparent, etc., see Sec. 2.2) allows a more detailed study of the properties of these ancestors.

5.1 The ancestors of the muons

Table 6 shows which parent contributes through its decay to the detected muons for the different primary gamma ray energies. At the lowest energy (1 GeV) about 89% of the muons are produced in decays of negative pions and 11% in decays of positive pions. This asymmetry can be explained by the different interaction cross sections at low energy of pions of either charge and by the fact that these pions are mainly produced in secondary interactions of neutrons (see below). Correspondingly, the probability for positive pions to interact instead of decay is larger than for negative pions. Above 3 GeV this asymmetry disappears and decaying kaons begin to contribute to the sea level muon flux. The latter contribution increases with energy and amounts to about 5% at 10 TeV.

It is interesting to note that at all energies FLUKA predicts the relative contribution of a positive kaon parent to be always larger than that of a negative kaon by about 20%. This effect is due to the properties of the DPM describing inelastic hadronic interactions within FLUKA. In particular, it is a feature of the Reggeon contribution which describes particle production by

Table 6
Fractional contributions to the parents of the muons which reach sea level. Values are given for different energies of the primary cosmic gamma ray.

E_γ (GeV)	π^+	π^-	K^+	K^-	neutral kaons
1	0.106	0.894	0.0	0.0	0.0
3	0.495	0.485	0.020	0.0	1.7×10^{-4}
10	0.492	0.489	0.011	0.007	9.8×10^{-4}
30	0.482	0.482	0.019	0.014	3.1×10^{-3}
100	0.478	0.477	0.022	0.018	4.4×10^{-3}
300	0.477	0.476	0.023	0.019	4.7×10^{-3}
1000	0.475	0.476	0.024	0.019	5.2×10^{-3}
3000	0.476	0.475	0.025	0.020	5.1×10^{-3}
10000	0.474	0.477	0.024	0.020	5.2×10^{-3}

one quark-diquark string stretched between a valence quark of the fluctuating photon and a diquark of a target nucleon. In this picture, kaon production involves the creation of a $s\bar{s}$ quark-antiquark pair and, in case of negative kaons, also the creation of an $u\bar{u}$ pair. On the other hand, positive kaons can be readily formed also by a u-quark of the fluctuating photon leading to the observed asymmetry.

The fractional contribution to the muon's grandparent is given in Table 7. The calculations for 1 GeV show distinctly different features. About 97% of the muons at sea level originate from mesons produced in interactions of neutrons in the close vicinity of the detector. At all other energies photoproduction dominates the picture with a contribution decreasing with energy from 99% at 3 GeV to 60% at the highest energy; the remaining fraction is mainly from pions.

5.2 Distributions of the number of generations

The distributions of the generation number of the grandparent of the sea level muon is shown in Fig. 8. The lower the energy of the primary gamma ray the smaller is the atmospheric shower resulting in a relatively narrow distribution. This distribution is peaked at generation one for energies below a few hundred GeV where the parent is mainly produced in a photoproduction process of the primary photon (see also Table 7). At higher energies secondary hadron interactions contributes significantly to the production of the parent. These secondary hadrons are mainly of third or fourth generation and cause a shift of

Table 7
Fractional contributions to the grandparent of the detected muon at sea level.

E_γ (GeV)	γ	p and $\bar{\text{p}}$	n and $\bar{\text{n}}$	π^+	π^-
1	1.7×10^{-3}	0.023	0.97	7.8×10^{-4}	4.9×10^{-3}
3	0.99	3.9×10^{-4}	5.0×10^{-3}	2.3×10^{-3}	2.1×10^{-3}
10	0.99	8.2×10^{-4}	1.9×10^{-3}	2.6×10^{-3}	2.7×10^{-3}
30	0.97	4.1×10^{-3}	5.3×10^{-3}	9.3×10^{-3}	9.2×10^{-3}
100	0.91	0.014	0.015	0.026	0.027
300	0.83	0.025	0.026	0.056	0.056
1000	0.73	0.037	0.041	0.091	0.090
3000	0.65	0.049	0.049	0.12	0.12
10000	0.60	0.054	0.057	0.13	0.14

the peak of the total distribution at TeV energies. The large tail at these energies which extends up to more than 100 generations reflects photoproduction processes of secondary photons in the large electromagnetic shower.

5.3 The muon production heights

The distributions of heights above sea level at which the detected muons were produced are shown for four primary energies in Fig. 9. As expected, at high energy there is a decrease in height with increasing energy of the primary gamma ray because of the logarithmic increase of the shower length. However, as the energy of the primary gamma ray decreases below 10 GeV, the energy of the muon parent is close to the minimum energy required for the muon to penetrate the blanket of air between its production and sea level. Hence, the most probable height of muon production begins to decrease with energies decreasing below 10 GeV. The blip-up near zero height, most pronounced in the 3 and 10 GeV distributions, represents the excess contribution from very low energy muons.

5.4 Radial distributions

The radial distributions of the muons at their production vertices and at sea level are shown in Fig. 10 for five different gamma ray energies. The radial distance, R, is defined with respect to the shower axis (z axis). The quantity dN/dA denotes the number of muons per unit area and per primary gamma

ray. The radial distributions of the production vertices are labeled "production."

All distributions extend to more than 10 km. Whereas the sea level distributions have a relatively flat shape below $R = 2$ km the production vertex distributions are increasing toward the shower axis and exhibit a change in slope or discontinuity at about 500 m which is most pronounced at low primary energy. This discontinuity indicates that two components with different shapes contribute. In order to further investigate this feature the muon production vertices were scored separately for those muons which originated from mesons produced in photoproduction processes and those from mesons produced by interactions of nucleons or other hadrons. The contributions from these components are shown for a primary energy of 10 GeV in Fig. 11. As can be clearly seen in the production vertex distributions (Fig. 11a) the photoproduction component dominates at small radii and the component due to interacting nucleons constitutes the tail at large R. The difference is smaller at sea level (Fig. 11b) due to multiple scattering of the muons in air.

5.5 Energy distribution of the muons

The kinetic energy distributions of muons at sea level and at the production vertex of these muons are shown in Fig. 12. Note, that the distributions are multiplied by the muon energy E_μ in order to enhance possible spectral structures at the higher energies. Whereas the sea level spectra are a smooth function with energy, the distributions of the muon energies at their birth exhibit a two-component structure. This two-component structure is again due to the superposition of muons from mesons generated in photoproduction processes and those from interacting hadrons. The two contributions are plotted separately in Fig. 13 for 10 GeV primary photon energy. It is clear that muons from photoproduction processes have a higher average energy.

6 Conclusions

Air showers caused by cosmic gamma rays with energies below 10 TeV were simulated using the Monte Carlo code FLUKA. The primary gamma rays were assumed to enter the atmosphere vertically. The reliability of FLUKA predictions in this energy region was explored by comparing its predictions for proton- and nuclei-induced air showers with experimental data; good agreement was found.

Many general properties of muon production in atmospheric gamma ray show-

ers were studied. As expected, most of the muons which reach sea level are decay products of charged pions; the contribution from kaons increases as the primary energy increases. Below 100 GeV primary energy, the decaying mesons are produced mainly in photoproduction processes. At higher energies, hadronic interactions of nucleons and pions contribute significantly. Variations in atmospheric pressure and temperature were investigated: A 3.0% increase in atmospheric pressure decreases the muon yield at sea level by 4.0% for 10 GeV primaries (3.2% at 1 TeV). Similarly, a 5.0% increase in the height-averaged temperature decreases the muon yield by 6.0% (3.6% at 1 TeV).

The main goal of the study was to determine the angular resolution for primary cosmic gamma rays from measurements of secondary muon angles at ground level. The angular distribution of muons at sea level narrows as the muon energy increases since low energy muons constitute the tails of the angular distributions. Thus, the angular resolution can be improved by eliminating the lower energy muons. The half-widths at half-maximum-height of the muon's projected angles are $\leq 1.1°$ above 100 GeV but rise to a value of $3.2°$ as the primary gamma ray energy is lowered to 10 GeV in the absence of the Earth's magnetic field deflection. Primary energies below 10 GeV essentially do not contribute muons at ground level. The effects of magnetic bending were considered separately as they depend on several factors; for example, they are more important in the East-down plane, for low primary energies, low muon energies, and larger North-components of the Earth's magnetic field.

The width of the angular distribution can be narrowed if the correlation of Θ_{xz} (angle projected onto the North-down plane) with x is taken into consideration (assuming the location of the core of the shower is measured). This narrowing can be accomplished either by eliminating large x and y values from the data or by compensating the measured angles knowing their expected mean values versus x and y as calculated from FLUKA.

Finally, the average muon angular correlation was calculated for a spectrum of primary gamma rays characterized by a spectral index. For a soft spectrum, e.g. a differential spectral index $\alpha = 3.0$, the average projected angular width (HWHM) is $2.6°$; for a mean value, $\alpha = 2.41$, the width is $1.6°$. If the spectrum is harder, e.g. $\alpha \leq 2.0$, the angular width improves to a constant value of $1.0°$. Corresponding values for a space angle resolution ($\delta\Theta_R$(HWHM)) are $\sqrt{2}$ larger. As mentioned above, if data with larger x and y values and/or the lower muon energies are removed, this angular correlation can be improved. This precise calculation of the angular correlations provides experiments which study the angular location of primary gamma ray sources by measuring muon angles with information on the angular resolution which is difficult to obtain experimentally.

Acknowledgments

Part of this work was supported by the Department of Energy under contract DE-AC03-76SF00515. Project GRAND is funded through grants from the University of Notre Dame and private donations.

References

[1] A. Fassò and J. Poirier, Phys. Rev. D **63**, 036002 (2001).

[2] The MILAGRO Collaboration, R. Atkins *et al.*, Nucl. Instr. Meth. in Phys. Res. A **449**, 478 (2000).

[3] J. Poirier *et al.*, in *Proceedings of the 26th International Cosmic Ray Conference (ICRC)*, Vol. 5, p. 304 (1999), World Wide Web: `http://www.nd.edu/~grand`.

[4] A. Fassò *et al.*, in *Proceedings of the 2nd Workshop on Simulating Accelerator Radiation Environments, CERN 1995*, edited by G.R. Stevenson, CERN Report TIS-RP/97-05, p. 158 (1997).

[5] A. Fassò *et al.*, in *Proceedings of the 3rd Workshop on Simulating Accelerator Radiation Environments, KEK 1997*, edited by H. Hirayama, KEK Proceedings 97–5, p. 32 (1997).

[6] A. Fassò, A. Ferrari, and P. R. Sala, *Electron-photon Transport in FLUKA: Status*, to appear in *Proceedings of the International Conference on Advanced Monte Carlo for Radiation Physics, Particle Transport Simulation and Applications, Monte Carlo 2000*, Lisbon, Portugal, 2000.

[7] A. Fassò *et al.*, *FLUKA: Status and Perspectives for Hadronic Applications*, to appear in *Proceedings of the International Conference on Advanced Monte Carlo for Radiation Physics, Particle Transport Simulation and Applications, Monte Carlo 2000*, Lisbon, Portugal, 2000.

[8] V. Patera *et al.*, Nucl. Instr. Meth. in Phys. Res. A **356**, 514 (1995).

[9] A. Ferrari, T. Rancati, and P. R. Sala, in *Proceedings of the 3rd Workshop on Simulating Accelerator Radiation Environments, KEK 1997*, edited by H. Hirayama (KEK Proceedings 97–5, 1997), p. 165.

[10] S. Roesler, W. Heinrich, and H. Schraube, Rad. Res. **149**, 87 (1998).

[11] G. Battistoni *et al.*, Astropart. Phys. **12**, 315 (2000).

[12] A. Capella *et al.*, Phys. Rep. **236**, 225 (1994).

[13] T. H. Bauer, R. D. Spital, and D. R. Yennie, Rev. Mod. Phys. **50**, 261 (1978).

[14] R. Engel, Z. Phys. C **66**, 203 (1995).

[15] S. Roesler, R. Engel, and J. Ranft, Phys. Rev. D **57**, 2889 (1998).

[16] M. Boezio *et al.*, Phys. Rev. D **62**, 032007 (2000).

[17] S. Roesler, W. Heinrich, and H. Schraube, *Monte Carlo simulation of the radiation field at aircraft altitudes*, in preparation.

[18] J. Kremer *et al.*, Phys. Rev. Lett. **83**, 4241 (1999).

[19] R. C. Hartman *et al.*, Astrophys. J. Suppl. Ser. **123**, 79 (1999).

[20] International Association of Geomagnetism and Aeronomy (IAGA), Division V, Working Group 8, *International Geomagnetic Reference Field - Epoch 2000, Revision of the IGRF for 2000 - 2005*, World Wide Web: `http://www.ngdc.noaa.gov/IAGA/wg8/wg8.html`

Figure Captions

1. Dependence of the negative muon flux produced by hadronic primaries on the depth in the atmosphere shown for different intervals of the muon momentum. FLUKA results (solid lines) are compared to data obtained by the CAPRICE experiment [16] (points). The comparison is shown for different intervals in muon momentum. The curves and data points for the first five momentum intervals were shifted by constant factors as indicated.
2. a) Energy spectra of positive and negative muons at 886 g/cm^2. FLUKA results (histograms) are compared to data obtained by the CAPRICE experiment [18]. $p_{\rm Lab}$ is the detected muon momentum. b) Muon charge ratio as a function of kinetic energy measured by the CAPRICE experiment [18] (points) and calculated with FLUKA (solid line).
3. Angular distribution of muons at sea level. Θ_{xz} is the angle of the detected muon projected onto the North-down or xz plane. The distributions are given for different primary photon energies and are normalized to unit area. Effects of the Earth's magnetic field are not included in this figure. Units of angle are in degrees.
4. (a) Angular distribution of muons at sea level for 10 GeV and (b) 10 TeV primary gamma ray energy. The distributions labeled "total" are the same as shown in Fig. 3. In addition, the contributions from muons with kinetic energies below 2 GeV and above 2 GeV are presented. Units of angle are in degrees.
5. Angular distributions of muons at sea level given for different intervals in the x coordinate. Results are shown for primary gamma ray energies of (a) 10 GeV and (b) 1 TeV. All distributions are normalized to unit area. Units of angle are in degrees.
6. (a) The figure shows the following quantities as a function of the primary gamma ray energy: the energy spectrum of primary gamma rays ($d\Phi_\gamma/dE_\gamma$) with a shape given by a differential spectral index $\alpha = 2.41$ and arbitrary normalization, the multiplicity of muons at sea level per primary gamma ray (N_μ/N_γ), the result of folding the multiplicity with the primary spectrum ($d\Phi_\mu/dE_\gamma = N_\mu/N_\gamma \times d\Phi_\gamma/dE_\gamma$; thin solid line with circles), the half-widths at half-maximum-height for all muon energies ($\delta\Theta_{xz}$(HWHM)) in degrees, and the result of folding these widths with $d\Phi_\mu/dE_\gamma$ (dot-dashed lines with diamond points). The calculated values are joined by lines to guide the eye. Note that all differential fluxes are multiplied by E_γ. (b) Average half-width at half-maximum-height for the angle projected onto the North-down plane as function of the spectral index of the primary spectrum; the ordinate is in units of degrees. Values for the space angle resolution ($\delta\Theta_R$(HWHM)) would be $\sqrt{2}$ times larger.
7. Muon angular distribution at sea level including the effect of the Earth's magnetic field for (a) 10 GeV and (b) 1 TeV primary gamma ray energy. The distributions are shown as a function of the muon's angle projected

onto the yz (East-down) plane, Θ_{yz}, and for three different geographic locations: (1) 42°N, 86°W (GRAND), (2) 36°N, 106°W (MILAGRO), and (3) 9°N, 100°E (maximum). The magnetic deflection for Θ_{xz} (North-down) is minimal and not shown. In addition, the distribution obtained without magnetic field (labeled "no field") is given. Units of angle are in degrees.

8. Distribution in the number of generations in the shower (see text) carried by the particles creating the parent-meson. FLUKA results are shown for different energies of the primary photon.
9. Distribution of the muon production heights. Results are given for primary photon energies of $3, 10, 100$, and 1000 GeV, respectively, and are normalized per primary photon. The top of the atmosphere is at 80 km in the calculations.
10. Radial distribution of the muon production vertices (i.e. meson decay vertices, dotted histograms) and of the muons at sea level (solid histograms). Results are given for primary photon energies of $3, 10, 100, 10^3$, and 10^4 GeV, respectively (from the bottom curve to the top). Values have been normalized per primary photon.
11. Radial distribution of the muon production vertices for 10 GeV primary photons at normal incidence. The distributions are given for (a) the muon production vertex and (b) for sea level. In addition to the total distribution, the contributions from different "parents" of the decaying meson are given. For example, the histograms labeled "photons" show the radial distributions of muons from mesons which were produced by photonuclear interactions. Distributions are normalized per primary photon.
12. Kinetic energy spectra of muons at their production vertices (dotted histograms) and at sea level (solid histograms). Values are normalized per primary photon.
13. Kinetic energy spectra of muons from 10 GeV primary photons at normal incidence. The spectra are shown for (a) the production vertex and (b) for sea level. In addition to the total spectra which are identical to those shown in Fig. 12, the contributions from different "parents" of the decaying meson are given (similar to Fig. 11).

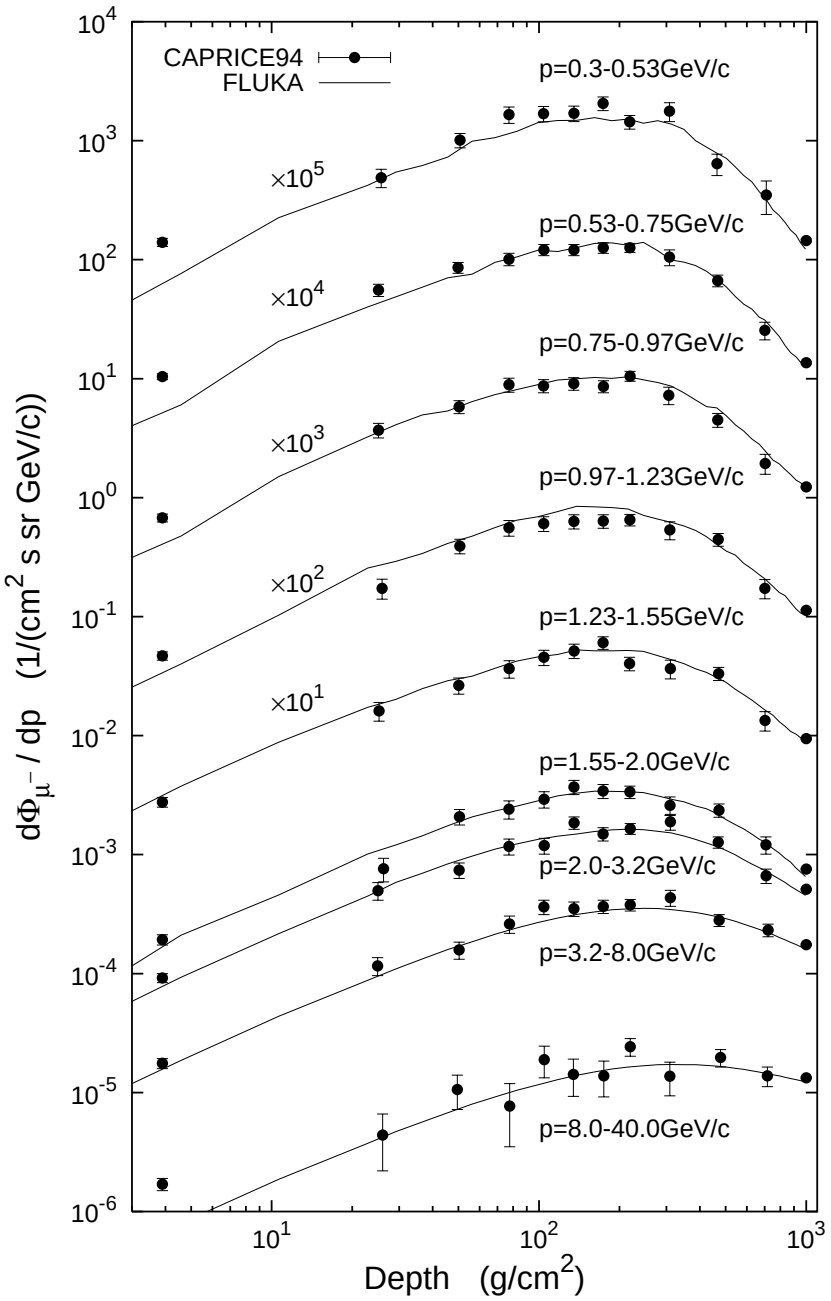
CAPRICE94
FLUKA
p=0.3-0.53GeV/c
×10^5
p=0.53-0.75GeV/c
×10^4
p=0.75-0.97GeV/c
×10^3
p=0.97-1.23GeV/c
×10^2
p=1.23-1.55GeV/c
×10^1
p=1.55-2.0GeV/c
p=2.0-3.2GeV/c
p=3.2-8.0GeV/c
p=8.0-40.0GeV/c
dΦμ− / dp (1/(cm2 s sr GeV/c))
Depth (g/cm2)

Fig. 1.

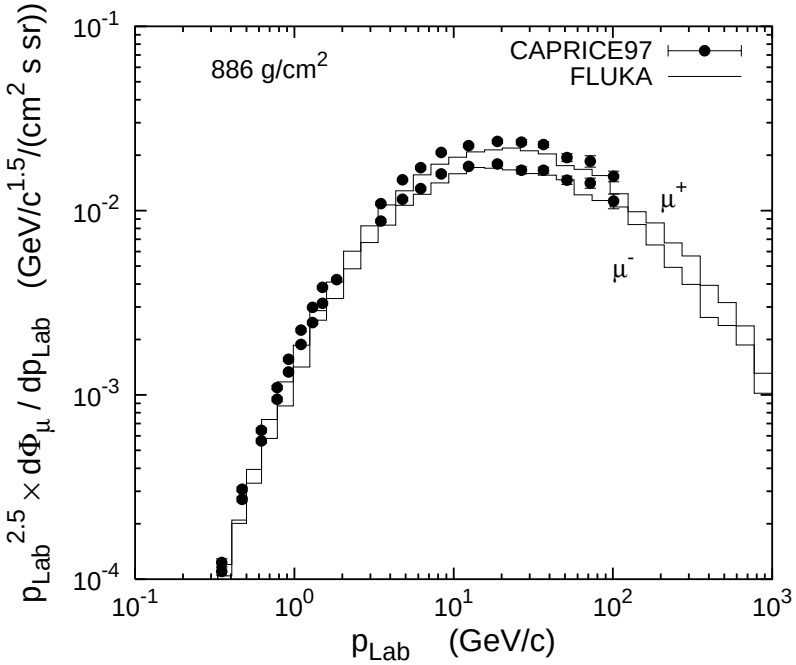
886 g/cm2
CAPRICE97
FLUKA
μ+
μ-
pLab2.5 × dΦμ / dpLab (GeV/c1.5/(cm2 s sr))
pLab (GeV/c)

(a)

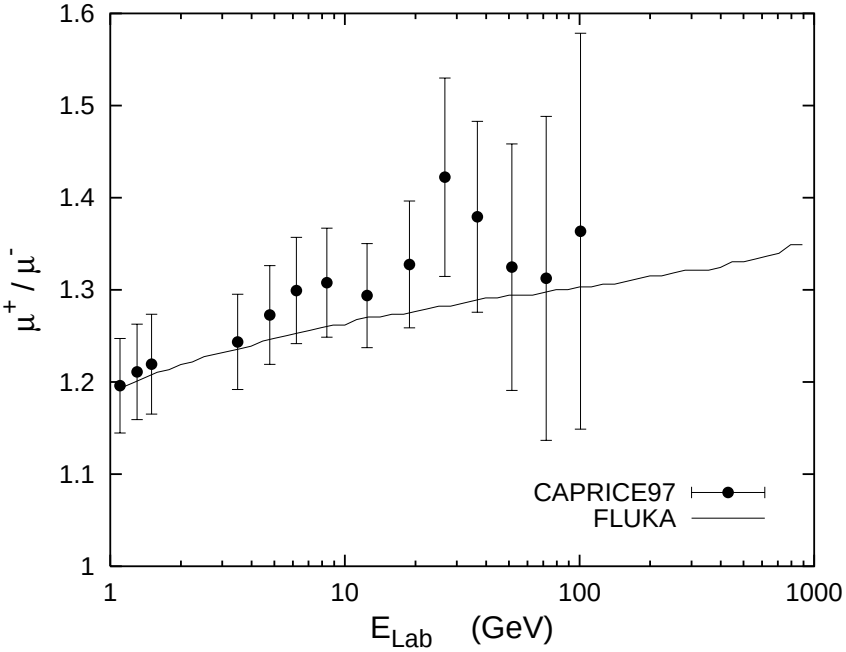
CAPRICE97
FLUKA
μ+ / μ-
ELab (GeV)

(b)

Fig. 2.

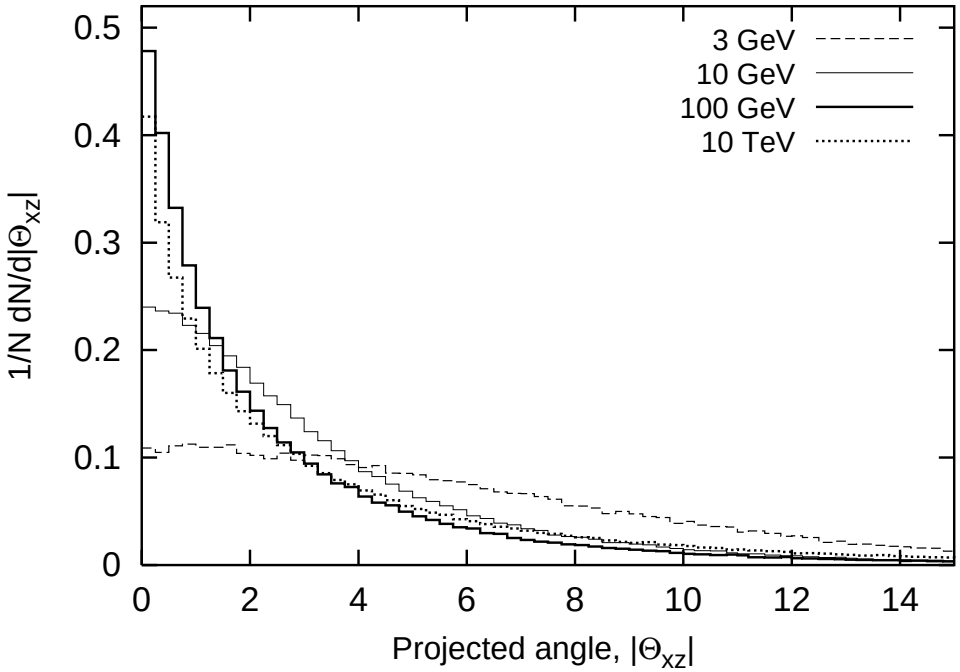
0.5
0.4
0.3
0.2
0.1
0
0
2
4
6
8
10
12
14
1/N dN/d|Θxz|
Projected angle, |Θxz|
3 GeV
10 GeV
100 GeV
10 TeV

Fig. 3.

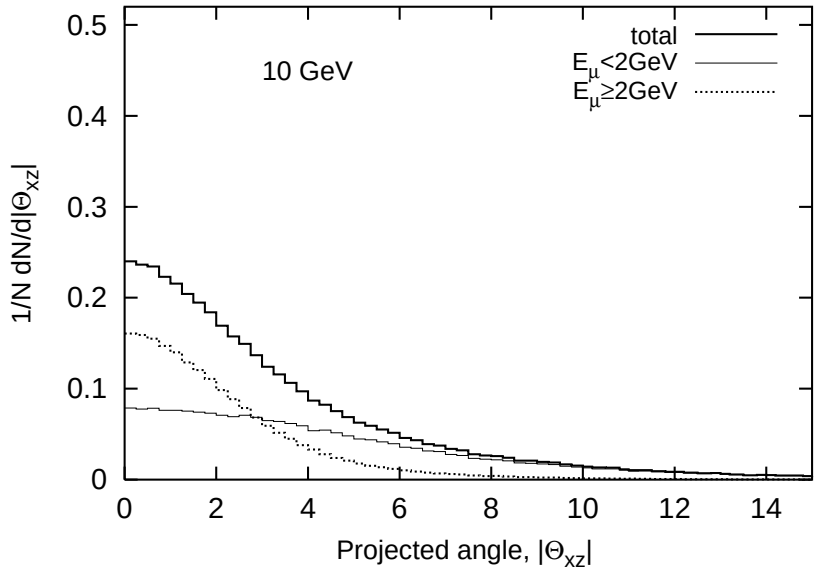
10 GeV
total
E_μ<2GeV
E_μ≥2GeV
1/N dN/d|Θ_{xz}|
Projected angle, |Θ_{xz}|
0
0.1
0.2
0.3
0.4
0.5
0
2
4
6
8
10
12
14

(a)

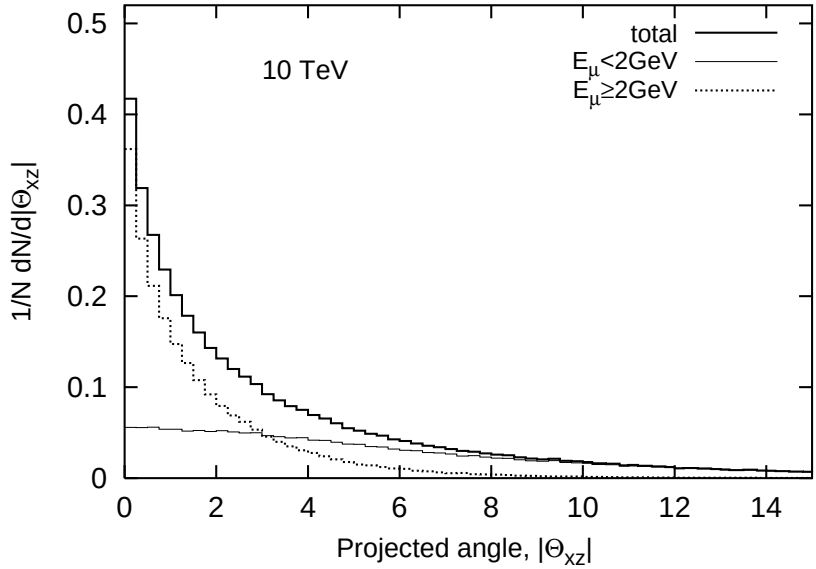
10 TeV
total
E_μ<2GeV
E_μ≥2GeV
1/N dN/d|Θ_{xz}|
Projected angle, |Θ_{xz}|
0
0.1
0.2
0.3
0.4
0.5
0
2
4
6
8
10
12
14

(b)

Fig. 4.

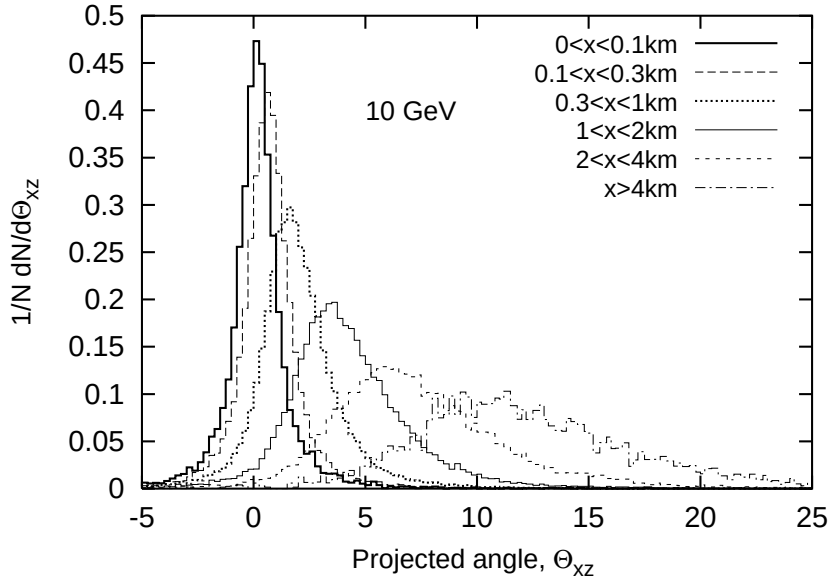
10 GeV
0<x<0.1km
0.1<x<0.3km
0.3<x<1km
1<x<2km
2<x<4km
x>4km
1/N dN/dΘxz
Projected angle, Θxz

(a)

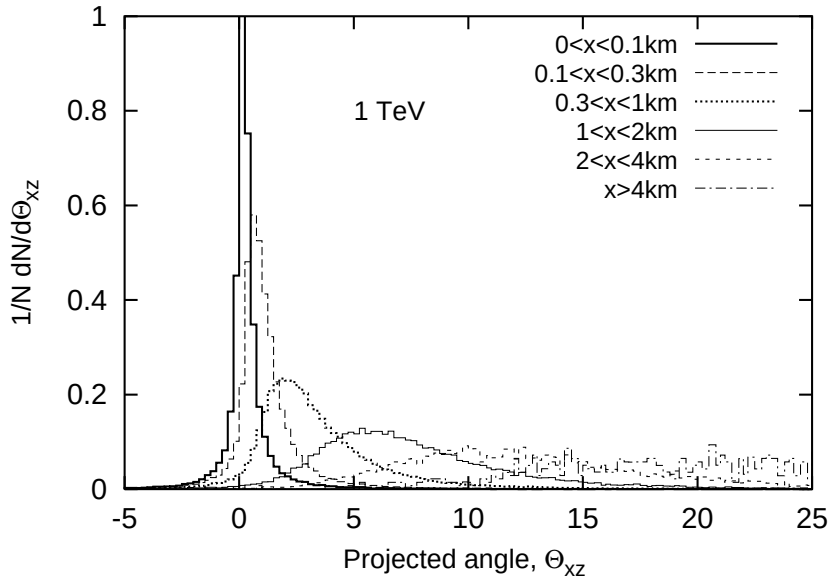
1 TeV
0<x<0.1km
0.1<x<0.3km
0.3<x<1km
1<x<2km
2<x<4km
x>4km
1/N dN/dΘxz
Projected angle, Θxz

(b)

Fig. 5.

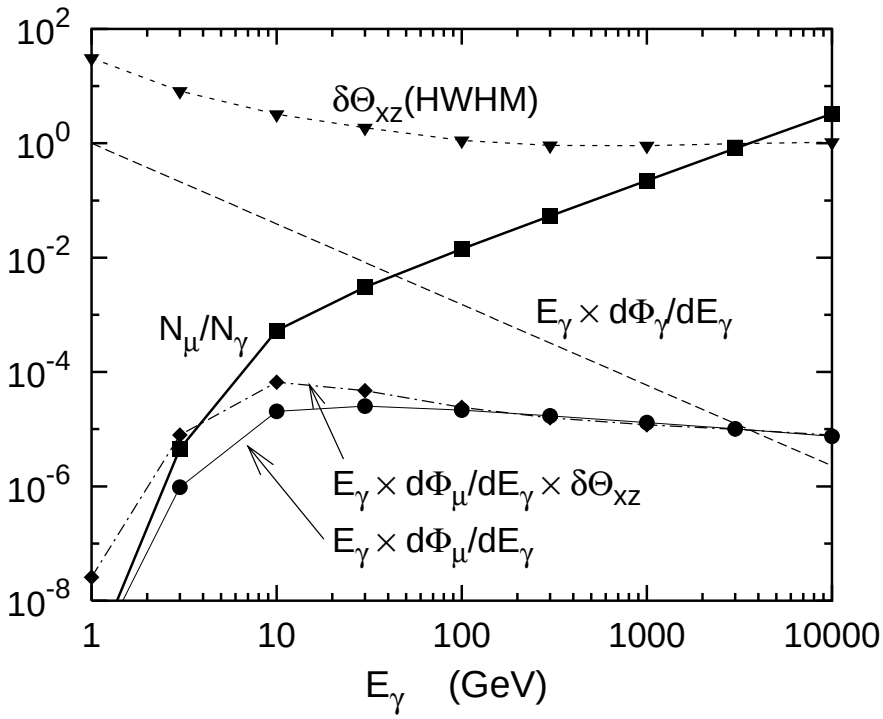
10^2
10^0
10^{-2}
10^{-4}
10^{-6}
10^{-8}
$\delta\Theta_{xz}$(HWHM)
N_μ/N_γ
$E_\gamma \times d\Phi_\gamma/dE_\gamma$
$E_\gamma \times d\Phi_\mu/dE_\gamma \times \delta\Theta_{xz}$
$E_\gamma \times d\Phi_\mu/dE_\gamma$
1
10
100
1000
10000
E_γ (GeV)

(a)

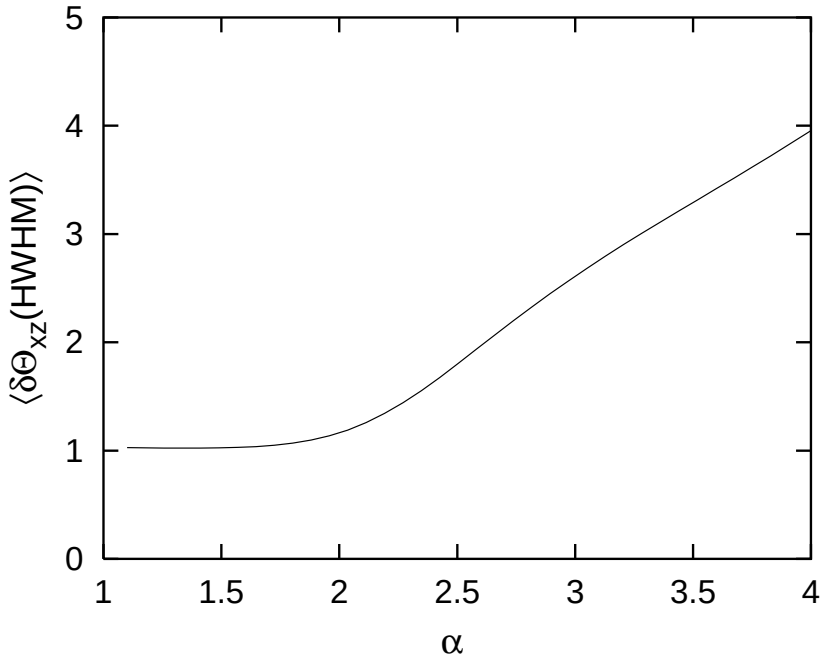
5
4
3
2
1
0
$\langle\delta\Theta_{xz}$(HWHM)$\rangle$
1
1.5
2
2.5
3
3.5
4
α

(b)

Fig. 6.

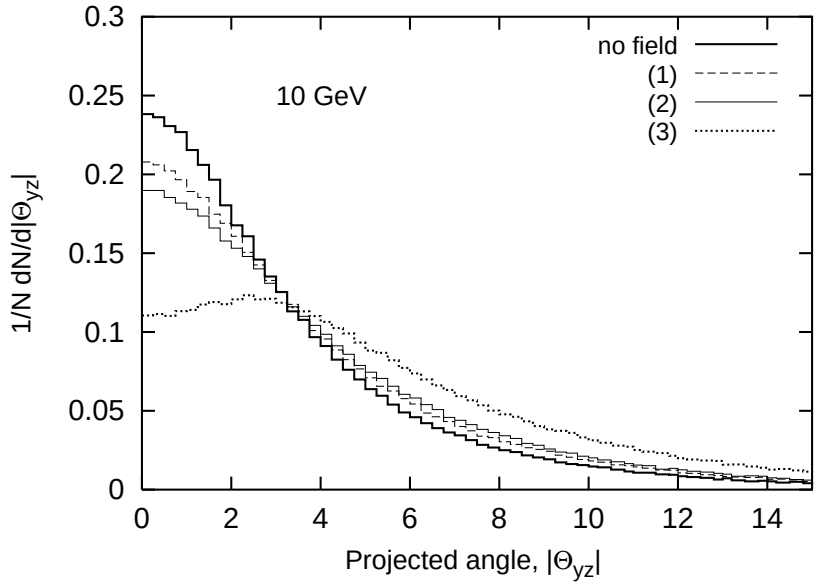
10 GeV
no field
(1)
(2)
(3)
1/N dN/d|Θyz|
Projected angle, |Θyz|
0
0.05
0.1
0.15
0.2
0.25
0.3
0
2
4
6
8
10
12
14

(a)

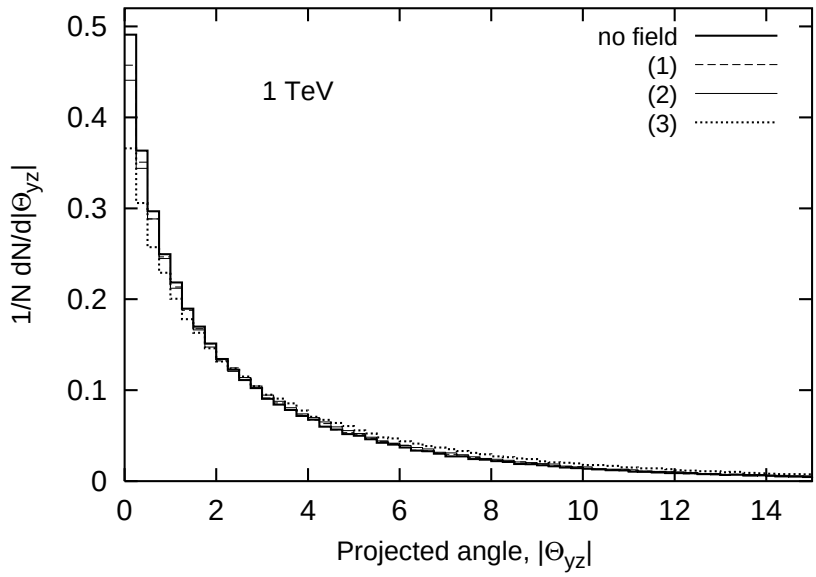
1 TeV
no field
(1)
(2)
(3)
1/N dN/d|Θyz|
Projected angle, |Θyz|
0
0.1
0.2
0.3
0.4
0.5
0
2
4
6
8
10
12
14

(b)

Fig. 7.

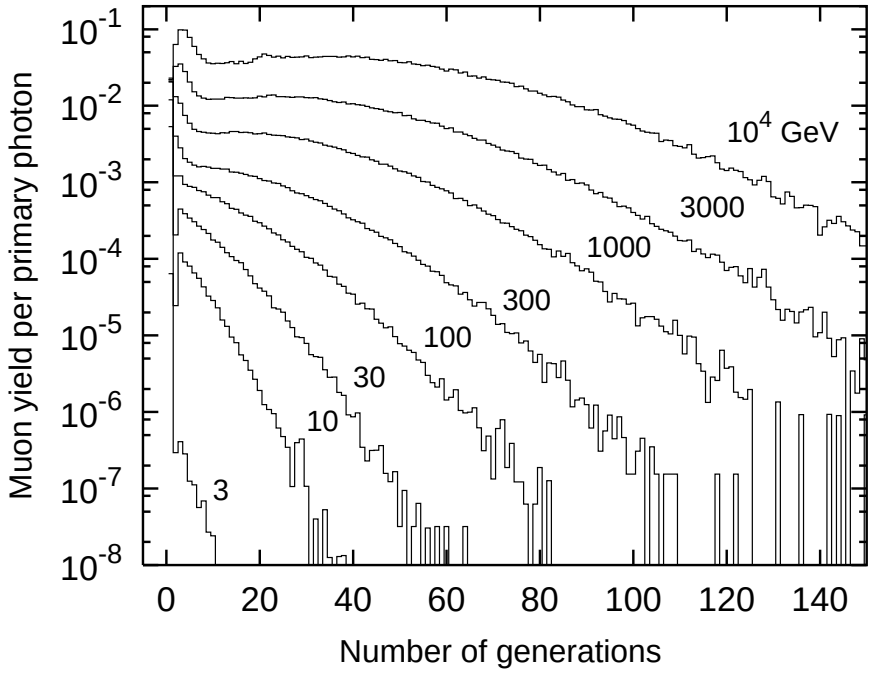
Muon yield per primary photon
Number of generations
10^{-1}
10^{-2}
10^{-3}
10^{-4}
10^{-5}
10^{-6}
10^{-7}
10^{-8}
0
20
40
60
80
100
120
140
10^4 GeV
3000
1000
300
100
30
10
3

Fig. 8.

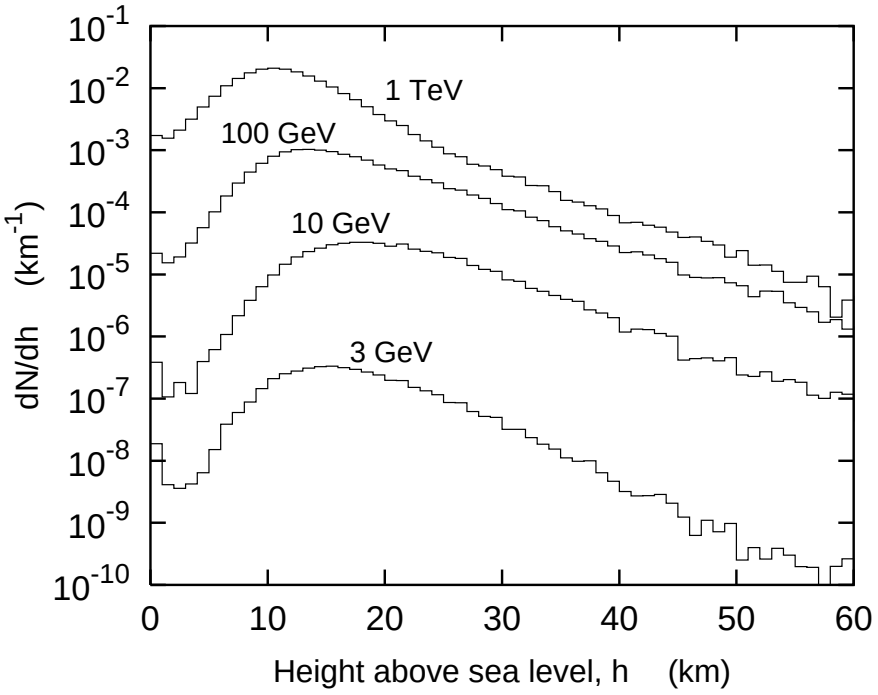
1 TeV
100 GeV
10 GeV
3 GeV
dN/dh (km-1)
Height above sea level, h (km)
10-1
10-2
10-3
10-4
10-5
10-6
10-7
10-8
10-9
10-10
0
10
20
30
40
50
60

Fig. 9.

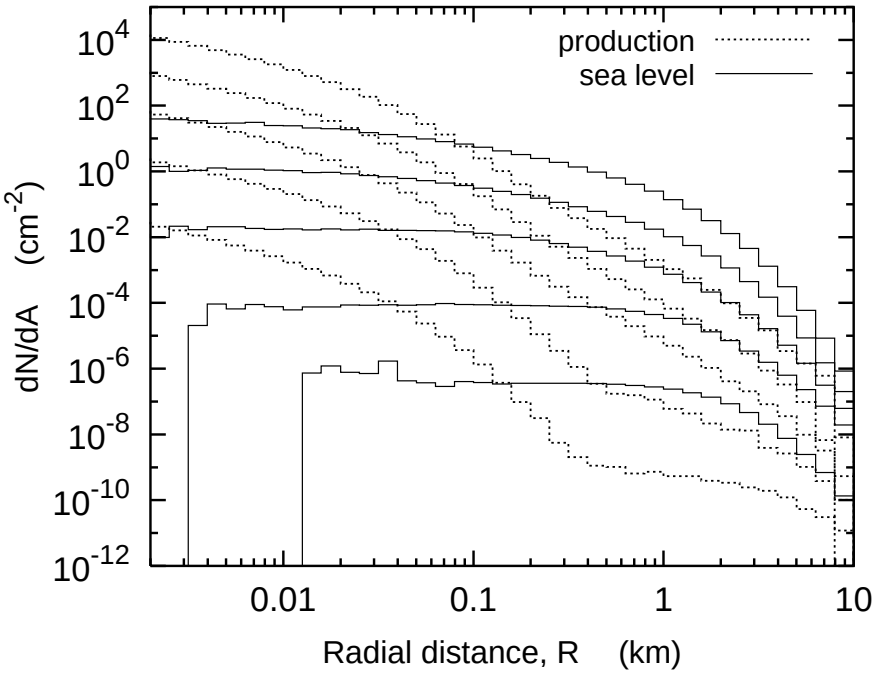
production
sea level
dN/dA (cm-2)
10^4
10^2
10^0
10^-2
10^-4
10^-6
10^-8
10^-10
10^-12
0.01
0.1
1
10
Radial distance, R (km)

Fig. 10.

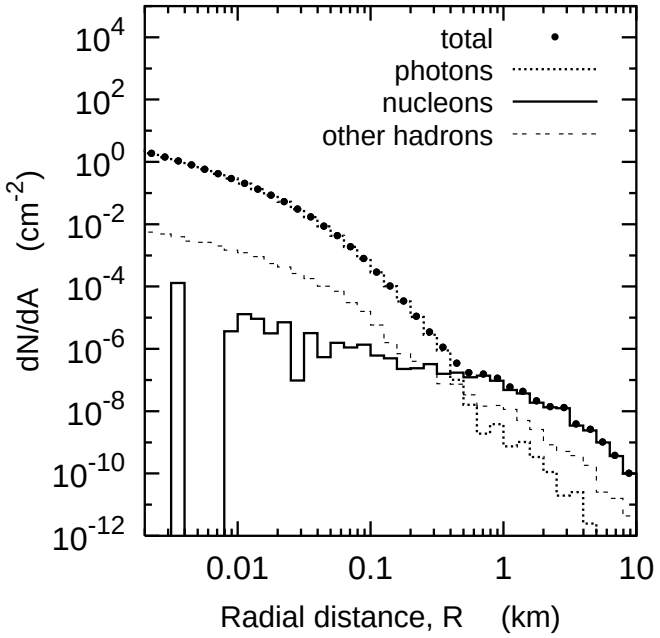
total
photons
nucleons
other hadrons
dN/dA (cm-2)
Radial distance, R (km)

(a)

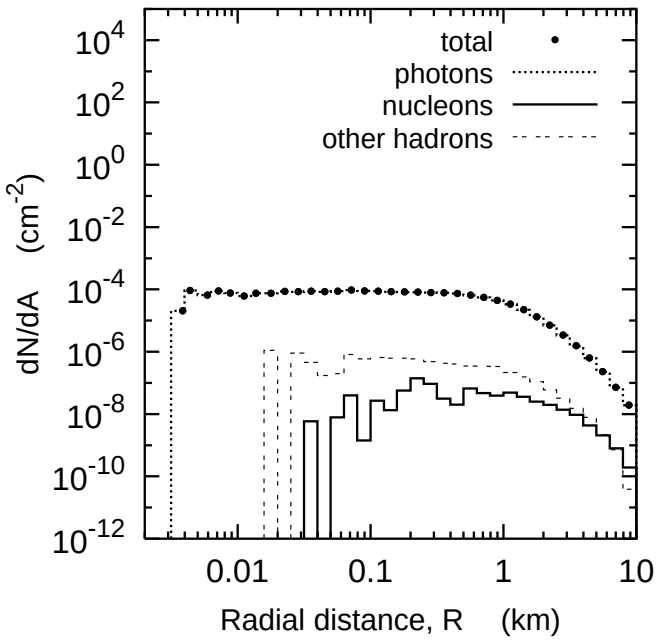
total
photons
nucleons
other hadrons
dN/dA (cm-2)
Radial distance, R (km)

(b)

Fig. 11.

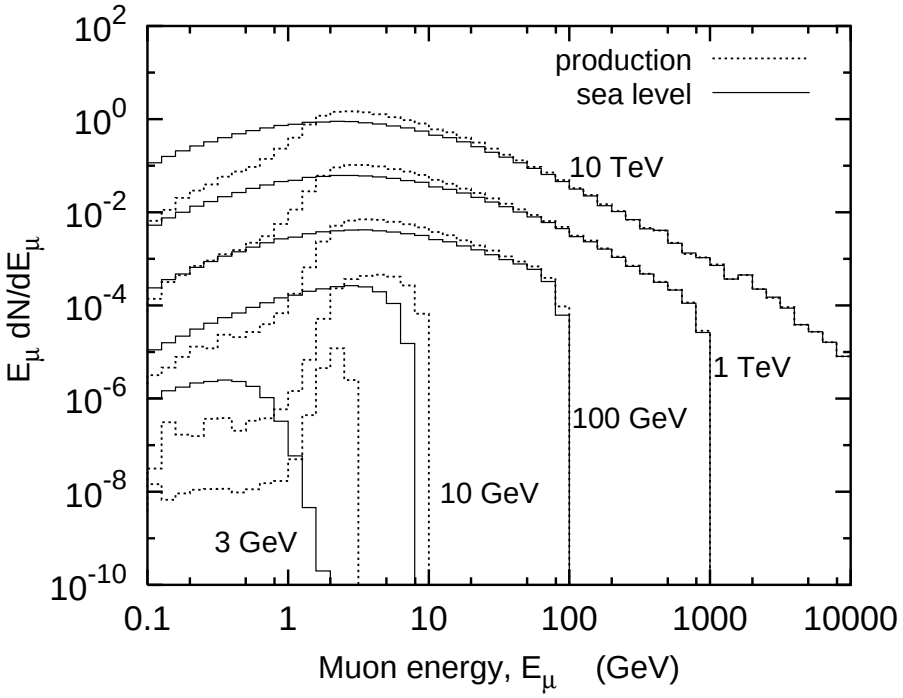
production
sea level
10 TeV
1 TeV
100 GeV
10 GeV
3 GeV
10^{2}
10^{0}
10^{-2}
10^{-4}
10^{-6}
10^{-8}
10^{-10}
E_μ dN/dE_μ
0.1
1
10
100
1000
10000
Muon energy, E_μ (GeV)

Fig. 12.

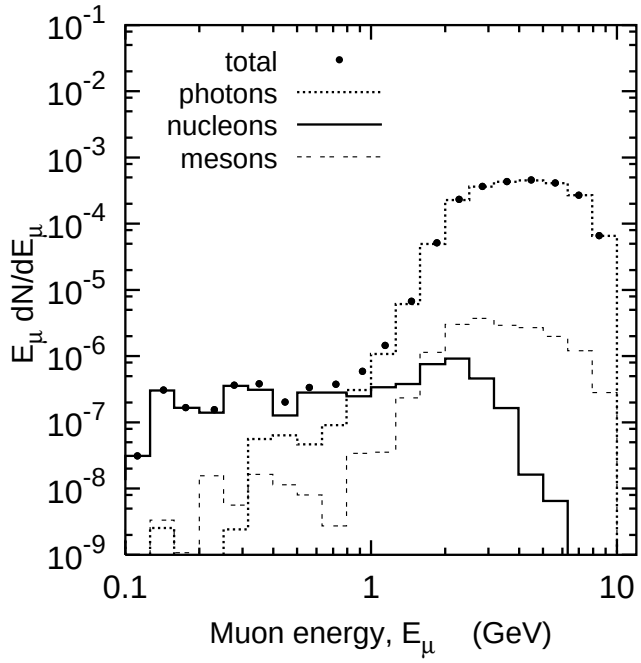
total
photons
nucleons
mesons
E_μ dN/dE_μ
Muon energy, E_μ (GeV)

(a)

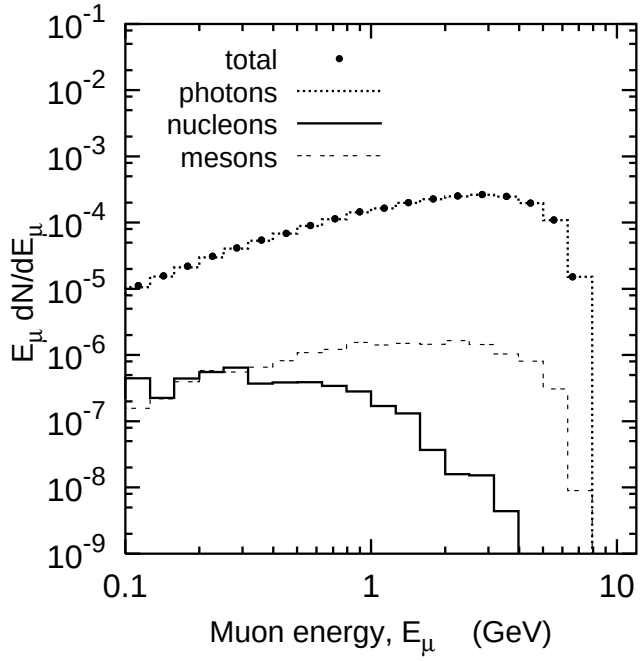
total
photons
nucleons
mesons
E_μ dN/dE_μ
Muon energy, E_μ (GeV)

(b)

Fig. 13.